Journal of Power Sources 372 (2017) 99–106

Contents lists available at ScienceDirect

Journal of Power Sources

journal homepage: www.elsevier.com/locate/jpowsour

Infiltrated $La_{0.4}Sr_{0.4}Fe_{0.03}Ni_{0.03}Ti_{0.94}O_3$ based anodes for all ceramic and metal supported solid oxide fuel cells

Jimmi Nielsen[a,*], Åsa H. Persson[a], Bhaskar R. Sudireddy[a], John T.S. Irvine[b], Karl Thydén[a]

[a] Department of Energy Conversion & Storage, Technical University of Denmark, DK-4000 Roskilde, Denmark
[b] School of Chemistry, University of St. Andrews, St. Andrews, Fife KY16 9ST, United Kingdom

HIGHLIGHTS

- High performing redox tolerant and corrosion resistant MS-SOFC anodes were developed.
- 0.77 Wcm^{-2} peak power density at 700 °C at a fuel utilization of 51% was obtained.
- A site deficient LST perovskites show good MS-SOFC processing characteristics.
- Ni:CGO infiltrated electrocatalyst coatings are stable on $La_{0.4}Sr_{0.4}Ti_{0.94}O_3$ surfaces.

ARTICLE INFO

Keywords:
Solid oxide fuel cell
Metal support
Lanthanum doped strontium titanate
Redox tolerance
Perovskite A site deficiency

ABSTRACT

For improved robustness, durability and to avoid severe processing challenges alternatives to the Ni:YSZ composite electrode is highly desirable. The Ni:YSZ composite electrode is conventionally used for solid oxide fuel cell and solid oxide electrolysis cell. In the present study we report on high performing nanostructured Ni:CGO electrocatalyst coated A site deficient Lanthanum doped Strontium Titanate ($La_{0.4}Sr_{0.4}Fe_{0.03}Ni_{0.03}Ti_{0.94}O_3$) based anodes. The anodes were incorporated into the co-sintered DTU metal supported solid oxide fuel cell design and large sized 12 cm × 12 cm cells were fabricated. The titanate material showed good processing characteristics and surface wetting properties towards the Ni:CGO electrocatalyst coating. The cell performances were evaluated on single cell level (active area 16 cm^2) and a power density at 0.7 V and 700 °C of 0.650 Wcm^{-2} with a fuel utilization of 31% was achieved. Taking the temperature into account the performances of the studied anodes are among the best reported for redox stable and corrosion resistant alternatives to the conventional Ni:YSZ composite solid oxide cell electrode.

1. Introduction

Solid oxide fuel cell (SOFC) and solid oxide electrolysis cell (SOEC) are well recognized as high efficiency electrochemical energy conversion devices. Generally, there is an interest to replace the conventional Ni:YSZ composite SOFC anode and SOEC cathode with an electrode that is more redox, coking and sulphur tolerant and which has a better long term stability in high steam containing atmosphere. Furthermore, for metal supported SOFC (MS-SOFC) the Ni of the Ni:YSZ composite electrode poses severe processing challenges. This is due to the solubility of Ni in e.g. ferritic stainless steel (FeCr) at high temperature and severe Ni coarsening when processed in a reducing atmosphere [1]. Technical University of Denmark (DTU) has due to the above mentioned MS-SOFC processing challenges developed a high performing infiltratable FeCr:YSZ composite MS-SOFC anode. However, the long term corrosion resistance of the FeCr:YSZ anode backbone needs to be improved [2]. For these reasons there has been intensive interest in developing novel anode materials and electrocatalysts. One possible solution is to skip Ni as part of the microstructured backbone and use ceramics exclusively (all ceramic). Modified $SrTiO_3$ perovskite materials has in this context been extensively explored due to their stability and potential high electronic conductivity (> 100 Scm^{-1}) in SOFC anode and SOEC cathode conditions [3,4]. In particular A site deficient lanthanum doped strontium titanates (LST) have shown, for a ceramic material, very high electronic conductivities and interesting properties such as good sintering characteristics [3,5] and the ability to be tailored for exsolution of electrocatalytic active (Mn, Ni, Fe, Cu) nanoparticles [6,7]. Recently, the materials $La_{0.4}Sr_{0.4}Fe_{0.06}Ti_{0.94}O_3$ and $La_{0.4}Sr_{0.4}Ni_{0.06}Ti_{0.94}O_3$, which exsolute Fe and Ni nanoparticles have been reported to be a step change towards realizing an alternative SOEC

* Corresponding author.
E-mail address: jini@dtu.dk (J. Nielsen).

http://dx.doi.org/10.1016/j.jpowsour.2017.10.066
Received 13 September 2017; Received in revised form 17 October 2017; Accepted 19 October 2017

cathode [7]. For further details on defect chemistry, structure, and exsolution properties of A-site deficient perovskites the reader is referred to references [3,4,6,7]. Previously, we have explored the use of infiltrated $SrTiO_3$:FeCr anodes for MS-SOFC [8]. However, the anode suffered some drawbacks such as it is difficult to process, microstructural densification upon operation and borderline electronic conductivity. However, it was demonstrated that titanates are excellent corrosion protection coatings for ferritic stainless steel.

In the present study we explore various novel Ni:CGO infiltrated MS-SOFC anodes. The anode backbone of the studied single cells are based on $La_{0.4}Sr_{0.4}Fe_{0.03}Ni_{0.03}Ti_{0.94}O_3$ (LSFNT) with possible exsolution properties of Fe and Ni nanoparticles. The backbone composition of the three studied anodes are 95% LSFNT/5% ScYSZ, 55% LSFNT/40% FeCr/5% ScYSZ and 20% LSFNT/60% FeCr/20% ScYSZ.

2. Experimental

2.1. Cell fabrication

The cell design is based on a multilayered structure fabricated by conventional ceramic processing techniques such as tape casting and screen printing. A metal support layer (ferritic stainless steel alloy (Fe22Cr)) and an anode backbone layer, comprising of an electronically conducting ceramic component ($La_{0.4}Sr_{0.4}Fe_{0.03}Ni_{0.03}Ti_{0.94}O_3$, LSFNT) and various vol.% of FeCr and ScYSZ particles, were tape casted individually and then laminated together with a tape casted electrolyte layer. The tape casting slurries consisted of, besides the metal and/or ceramic powders, an organic system containing solvent, binder, plasticizer, and other additives (such as pore formers) needed for the fabrication of porous and/or dense layers. The electrolyte was based on ZrO_2 co-doped with Sc_2O_3 and Y_2O_3 (from here on referred to as ScYSZ). The LSFNT material was fabricated with solid state route and supplied by the company KCERACELL. The laminated layers comprising the half cell (metal support, anode backbone layer, and electrolyte) were air debinded to remove the organics from the tapes. The debinding step was followed by a co-sintering step, using a proprietary procedure, above 1100 °C in a reducing atmosphere (H_2/Ar). After co-sintering, the electrocatalytically active phase, comprising a precursor solution for $Ce_{0.8}Gd_{0.2}O_{1.9}$ (CGO20) and Ni, was infiltrated into the porous structure of the half cell. The procedure followed for the infiltration of electrocatalysts is described elsewhere [9,10]. The infiltrated oxide phases amounted to approximately 3 wt.% of the half cell and is hereafter referred to as Ni:CGO. Next, a 1 μm thick $Ce_{0.9}Gd_{0.1}O_{1.95}$ (CGO10) cathode barrier layer (CBL) to prevent interdiffusion was deposited with PVD, as described by Klemensø et al. [11]. A cathode with a composition of $(La_{0.6}Sr_{0.4})_{0.99}CoO_{3-\delta}$ (LSC) was applied by screen printing. The cathode layer was fired in situ during cell testing as described in the subsequent section 2.2.

2.2. Electrochemical characterization

The single cells was cut out of large 12 cm × 12 cm cells and had a 54 × 54 mm cell area with an active area of 16 cm^2 (defined by the screen-printed cathode layer). The cells were tested in an alumina housing used for conventional anode-supported cells, and the test house and positions of voltage probes and current pick-up points were as described in Ref. [12]. A flat Ni net was used as a current collector on the anode side, and Au net was used on the cathode side. The cell rested directly on the flat Ni net with the edges being sealed with glass. The fuel gas was distributed from one side to the other via milled gas trenches in a 1 mm thick Ni block, which was embedded in the alumina test housing. On top of this arrangement, on the cathode side, an alumina block with the flat current collecting Au nets was put and a weight of 4 kg was applied. No sealing was used on the cathode side since the gas was distributed from the middle of the cathode and outwards via milled gas trenches in the alumina top block. The cells were heated to 800 °C for 5 h in order to seal the cells and sinter the cathode before the performance and durability tests were started. During start up air was supplied to the cathode side and dry 9% H_2 in N_2 to the anode side (to prevent corrosion of the metal support at the elevated temperature).

Polarization curves and impedance data were collected in the temperature range 650–750 °C with 4% and 20% humidified H_2 on the anode side, and air or oxygen on the cathode side. The fuel and air flows were maximum 1.5 and 8.75 Nl $h^{-1}cm^{-2}$, respectively. The electrochemical impedance (EIS) data was recorded using a Solartron 1260 Gain-Phase Analyser and a Solartron 1255B frequency response analyser (Solartron Instruments, Houston, Texas). Galvanostatic durability tests were conducted at 650 °C at a current density of 0.25 Acm^{-2} with 4% humidified hydrogen as fuel and air as oxidant gas. The fuel and oxygen utilization was below 15%. The cells were characterized before, during and after the durability tests with EIS measurements.

2.3. Microstructural characterization

The microstructure of the various cell samples was investigated using polished cross-sections, while the nanostructured electrocatalyst coatings were investigated by looking at fractured cell cross sections. The polished cross-sections were prepared by vacuum embedding the samples in Struers epoxy resin (Epofix); ground using SiC paper; polished using 6, 3 and 1 μm diamond paste, and then carbon coated to eliminate surface charging. Scanning electron microscopy (SEM) imaging with backscattered electrons was performed using a Hitachi TM1000 tabletop SEM. For high resolution SEM the standard backscattered electron detector and the energy selective detector in a Merlin (Zeiss, Germany) FEG-SEM was used.

3. Performance considerations

For modern high performance SOFC electrodes three main parameters are of importance the electrochemical reaction kinetics, the electronic conductivity and the ionic conductivity. The coupling hereof is usually on a macroscopically scale electrochemically described by a so-called transmission line as reviewed in Ref. [13]. For further details and experimental verification of such modelling the reader is referred to the given reference and the references herein. The mass transport properties are in this context considered to be part of the electrochemical reaction kinetics. For utilization of the large inner surface of porous electrodes and hence achieve high and durable performance modern porous electrodes need to possess the above mentioned characteristics. In practical terms it also needs to be a certain balance between these properties. The optimal would be one material which satisfies all these 3 characteristics and in addition have sufficient chemical stability for durable performance and a SOFC compatible thermal expansion coefficient (TEC) for mechanical stability. However, such materials have so far not been identified. A more pragmatic approach is composites where materials, which are excellent in one area such as ionic conductivity, electronic conductivity or electrocatalysis are put together and engineered to form an electrode with a good balance between physical properties such that it overall results in excellent and durable performance. Nonetheless, in this approach chemical compatibility among employed materials may also become an issue of concern. For the anode composition 95% LSFNT/5% ScYSZ the electronic conductivity is supplied by LSFNT, while ionic and electrocatalytic activity is supplied by the infiltrated Ni:CGO electrocatalyst. The 5% ScYSZ is put into the anode with the aim of strengthen the electrolyte/anode adhesion. In the composition 55% LSFNT/40% FeCr/5% ScYSZ the electronic conductivity is improved by the presence of FeCr metal, while for the last composition 20% LSFNT/60% FeCr/20% ScYSZ both the electronic conductivity by presence of FeCr and the ionic conductivity by presence of ScYSZ is improved. Finally, the microstructure in terms of porosity is also an important factor, since this influence the electrocatalyst loading. This is discussed further in the

following section 4.1.

4. Results and discussions

4.1. Microstructure and composition

The microstructure of the studied anode compositions are shown in Fig. 1. It can be seen that the 95% LSFNT/5% ScYSZ anode has the densest microstructure (cell A). This is followed by the 55% LSFNT/40% FeCr/5% ScYSZ anode (Cell B), while the 20% LSFNT/60% FeCr/20% ScYSZ anode has the most open microstructure (Cell C). The different phases can be identified by their chemical contrast when imaged by backscattered electrons in SEM. For example the bright white spots and areas are Ni:CGO electrocatalyst, from which it can also be seen that the electrocatalyst is not entirely evenly distributed. The pore size and its distribution is expected to effect the amount and the distribution of Ni:CGO electrocatalyst deposition. A higher porosity will accumulate a higher amount of liquid and thus electrocatalyst upon an infiltration cycle. For these reasons it is expected that higher loadings and thus thicker electrocatalyst coatings will be the result for a highly porous microstructure with large pores. In the case of a broad pore size distribution, there seems to be a tendency that there is an accumulation of electrocatalyst associated with the smaller pores. Thus, the electrocatalyst is not evenly distributed within the microstructure. A possible

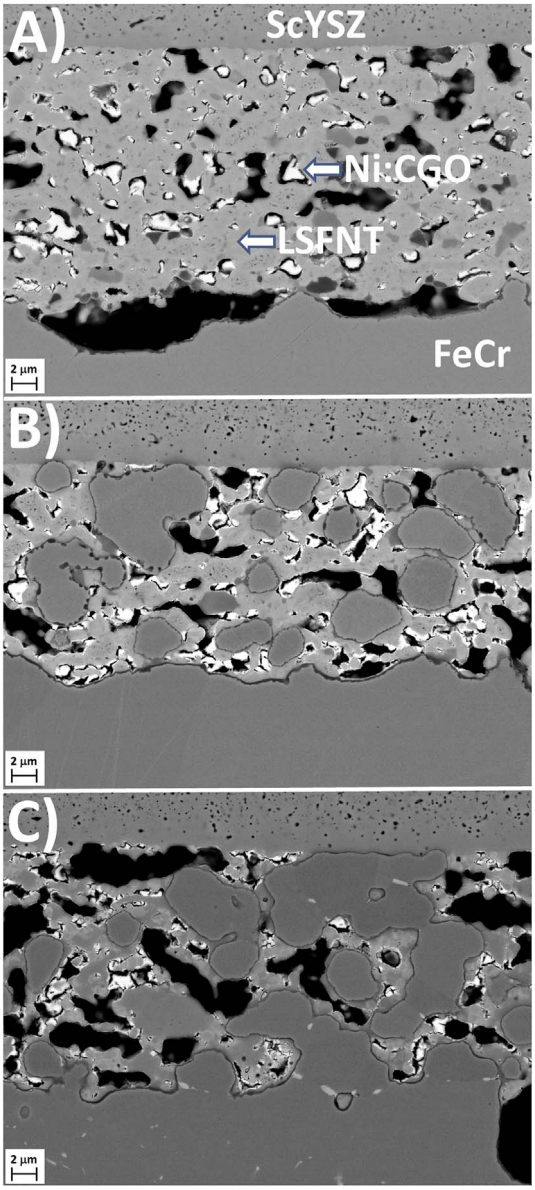

Fig. 1. Cross sectional SEM micrographs of studied infiltrated anodes with different anode backbone compositions **A)** 95% LSFNT/5% ScYSZ **B)** 55% LSFNT/40% FeCr/5% ScYSZ **C)** 20% LSFNT/60% FeCr/20% ScYSZ.

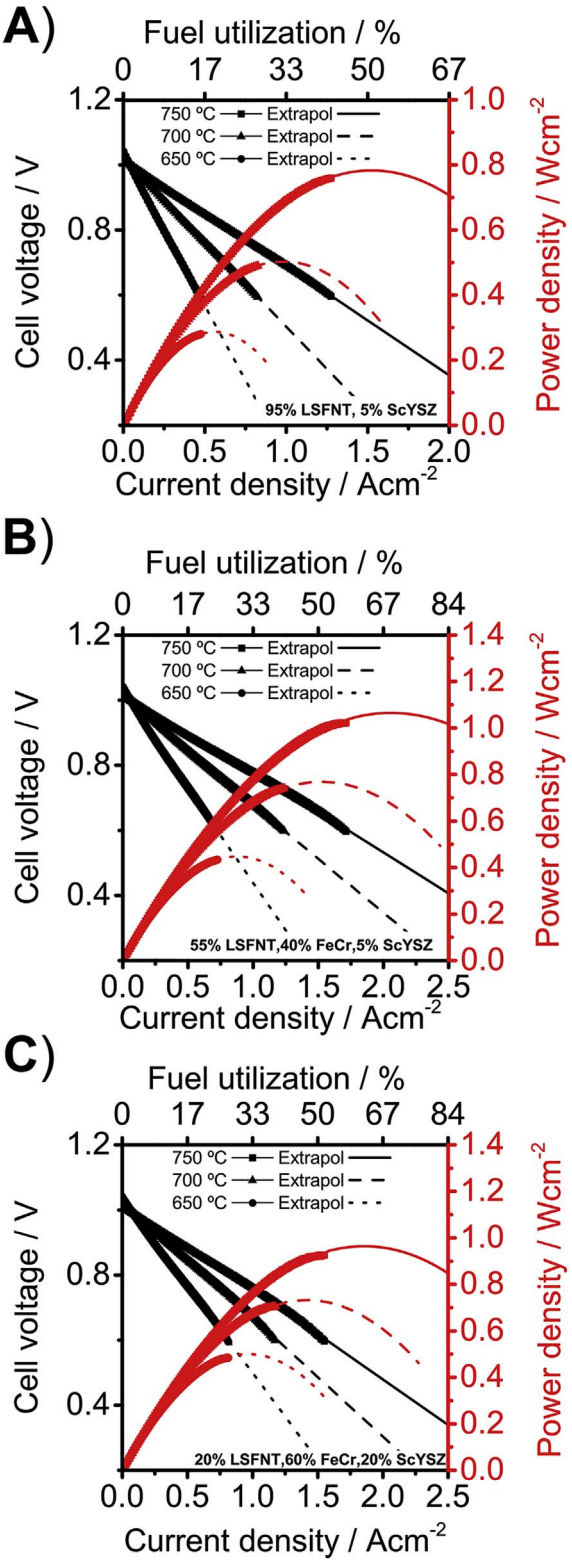

Fig. 2. Performance characteristics at 650 °C, 700 °C and 750 °C with air as oxidant and 20% humidified hydrogen as fuel of MS-SOFCs with different anode backbone compositions and microstructure. **A)** 95% LSFNT/5% ScYSZ **B)** 55% LSFNT/40% FeCr/5% ScYSZ **C)** 20% LSFNT/60% FeCr/20% ScYSZ.

explanation could be that the capillary forces has a more predominant effect for the smaller pores. Therefore upon water evaporation when the sample is heated after infiltration, the water within the smallest pores is the last to evaporate. Since the concentration increases as water is evaporated a larger electrocatalyst deposition will take place in association with the smallest pores. For a more even electrocatalyst deposition it therefore seems desirable with a narrow pore size distribution. However, for other purposes such as a given desirable sintering characteristics this may not be feasible.

4.2. Performance of the tested cells

The performance of the cells A, B, C at 750 °C, 700 °C and 650 °C are presented in Fig. 2. The performance characteristics are summarized in Table 1. Since single cell testing is used for performance evaluation, the fuel utilization (FU) is not insignificant. This is unlike button cell testing where the cells are flushed with fuel and the effect of fuel utilization is suppressed. This is feasible as the active area is very small (typically ≤ 0.5 cm^2). In addition many variations of button cell setups exist with different gas flow configurations. Most commonly the gas is flushed perpendicular onto the cell and therefore the gas is directly forced into the porous structure of the cell resulting in a situation with favorable gas mass transport. In the used single cell testing, the flow configuration is similar to what will be present in a stack that is plug flow. Thus, the condition in single cell testing mimics stack conditions and the measured performance of the cell will therefore be very close to what can be expected in a stack environment. Nonetheless, regardless of test setup it is important when reporting a performance also to specify the fuel utilization. Despite important it is often not done. The importance and impact of fuel utilization has been considered before in Ref. [12]. In here, a methodology for compensating for the fuel utilization has been suggested. An exact compensation of fuel utilization is not feasible, but estimation of a conservative first approximation is feasible. Basically, the methodology attempts to compensate for the change in Nernst potential as the fuel is utilized. Area specific resistances (ASRs) corrected by this methodology is specified as ASR_{corr} in Table 1. As can be seen, the polarization characteristics of the cells are very linear when 20% humidified hydrogen is used as fuel. As a DTU standard, cells are usually not operated below 0.6 V, which historically is meant as a safety precaution not to harm the cell. However, there is no indication that it is not feasible to operate the cells below 0.6 V. To obtain the peak power density, which often is used for performance comparison, the measured polarization curves are therefore linearly extrapolated. Furthermore, assumption of linear polarization characteristics ASR_{corr} has been used in the estimation of the associated fuel utilization corrected peak power density (PPD FU corr in Table 1). These fuel utilization corrected performance characteristics are what should be compared with button cell evaluations. Thus, compensation of fuel utilization offers a platform for comparison of performances among different studies within the literature. Another quite common performance benchmarking is the performance at 0.7 V and within the present study we have chosen 700 °C. From the results in Fig. 2 summarized in Table 1, cell A with all ceramic anode composition (95% LSFNT/5% ScYSZ) performs the worst with a power density of 0.450 Wcm^{-2} at benchmarking conditions with FU = 22%. At benchmarking conditions both cell B and cell C show similar performance with a power density of 0.650 Wcm^{-2} with FU = 31%. However, at a higher temperature of 750 °C cell B performs slightly better with a performance of 1.07 Wcm^{-2} at a FU 69%, while cell C shows a slight better performance at lower temperature of 650 °C with 0.52 Wcm^{-2} at a FU 32%. Nonetheless, the performance of cell B and cell C can in a larger context be considered identical. Thus, the improved ionic conductivity by the presence of ScYSZ does not seem to lead to any significant improvement in performance. For Ni:CGO electrocatalyst coated ScYSZ surfaces to be electrochemically active the electrons needs to be supplied by the Ni:CGO electrocatalyst coating and transported over distances of micrometers (size of ScYSZ particles). Seemingly, this is not a favorable mechanism as significant performance improvement is not realized. The phase fraction of 20% ScYSZ is also below the percolation limit. Nonetheless, the performance of cell C with ASR_{corr}(650 °C) = 0.511 Ωcm^2 is similar to the DTU SoA design with an infiltrated FeCr/YSZ anode backbone and an ASR_{corr}(650 °C) ~ 0.5 Ωcm^2 [2], where a YSZ percolated network is present. In conclusion, it seems that the presence of ionic conducting stabilized zirconia based materials have little impact on the performance. Instead it seems more open microstructures, which enables higher Ni:CGO electrocatalyst coatings have a much higher impact on the performance. For example versions of DTU SoA architecture with more open microstructures have been shown to have ASR_{corr}(650 °C) values as low as 0.35 Ωcm^2 [14]. Recently, M. Tucker has also shown for cells with comparable electrode

Table 1
Summary of performance characteristics of the studied cells A, B and C. The used abbreviations are as follows FU = fuel utilization, ASR = area specific resistance, ASR_{corr} = fuel utilization corrected ASR, PPD = peak power density, PPD_{corr} = fuel utilization corrected PPD.

Cell type	A	B	C
Anode backbone composition	95% LSFNT 5% ScYSZ	55% LSFNT 40% FeCr 5% ScYSZ	20% LSFNT 60% FeCr 20% ScYSZ
Performance characteristics 750 °C			
ASR / Ωcm^2	0.325	0.236	0.253
ASR_{corr} / Ωcm^2	0.294	0.205	0.222
PPD (extrapol) / Wcm^{-2}	0.780, FU 51%	1.07, FU 69%	0.960, FU 62%
PPD FU corr / Wcm^{-2}	0.881	1.264	1.167
Performance characteristics 700 °C			
ASR / Ωcm^2	0.478	0.344	0.352
ASR_{corr} / Ωcm^2	0.450	0.315	0.323
PPD (extrapol) / Wcm^{-2}	0.503, FU 33%	0.770, FU 51%	0.730, FU 48%
PPD FU corr / Wcm^{-2}	0.589	0.842	0.821
Performance characteristics 650 °C			
ASR / Ωcm^2	0.929	0.600	0.539
ASR_{corr} / Ωcm^2	0.900	0.572	0.511
PPD (extrapol) / Wcm^{-2}	0.287, FU 19%	0.448, FU 29%	0.520, FU 32%
PPD FU corr / Wcm^{-2}	0.302	0.475	0.532
Benchmarking @ 700 °C, 0.7 V			
Benchmarking / Wcm^{-2}	0.450, FU 22%	0.649, FU 31%	0.650, FU 31%
Benchmarking corr / Wcm^{-2}	0.519	0.734	0.725

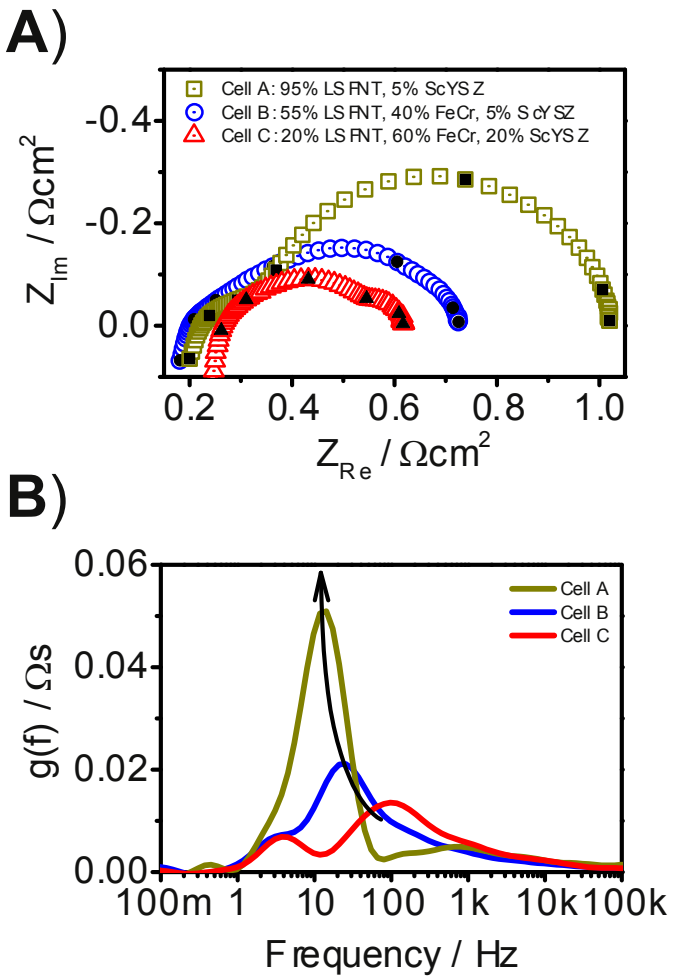

Fig. 3. Impedance data at open circuit voltage at 650 °C with air as oxidant and 20% humidified hydrogen as fuel **A)** Impedance of the studied cells with different anodes. The solid black points indicate the frequencies 96.85 kHz, 9.685 kHz, 968.5 Hz, 96.85 Hz, 9.685 Hz, 968.5 mHz, 96.85 mHz. **B)** Distribution of relaxation times visualization of impedance data of the studied cells.

architectures and electrocatalysts that boosting infiltrated electrocatalyst loadings leads to significant performance improvements [15]. Fig. 3A shows the impedance spectra of the three studied cells at 650 °C, with air as oxidant and 20% humidified hydrogen as fuel. Any difference in the spectra is expected to be due to the anode since the remaining cell layers are the same. From the spectra is possible to see differences in both the serial resistance R_s and the polarization resistance R_p. The high frequency interception with the real axis reflects the AC serial resistance R_s, which consists of contributions from possible ohmic losses from current collection, electrolyte resistance and electrode current constrictions. Any difference can therefore only originate from current collection of the electronic conducting parts within the anode layer and the electrolyte/anode current constriction resistance. The current constriction resistance depends on the area and density of contact points between the LSFNT and FeCr particles with the ScYSZ electrolyte [16]. The presence of ScYSZ and the higher porosity of cell C (20% LSFNT/60% FeCr/20% ScYSZ) will result in a higher electrolyte/anode interfacial current constriction resistance and may explain the observed higher serial resistance R_s. As mentioned previously in section 3, the coupling between electronic conduction, ionic conduction and an electrochemical reaction will lead to a so-called transmission line response. The impedance shape of such a transmission line response is for most practical cases a skewed semicircle in a Nyquist plot [10,13,14]. From inspection of the impedance spectra shapes, this seems to be the case for cell A (95% LSFNT/5% ScYSZ) and cell B (55% LSFNT/40% FeCr/5% ScYSZ). However, cell C distinguish itself by first of all having the highest polarization resistance and secondly by a different shape, that is dominated by a semicircle shaped like contribution. The relatively large semicircle like shape necessarily has to be associated with the anode and indicates that the electrochemical reaction is very much restricted to the anode/electrolyte interface. Thus, the electrode electrochemical utilization thickness is very limited. Since the serial resistance R_s is as expected (close to that of cell B and cell C), the electronic conductivity is sufficient meaning it is presumably the ionic conductivity of electrode, which is insufficient and limiting the extension of electrochemical reaction zone and hence the performance. Previous studies on STN based anode backbones also showed a large and semicircle like impedance response, where it was clear that the multifunctional ionic, electronic conducting Ni:CGO electrocatalysts coating was unstable with the result of a non-percolated island like coating structure [8]. From SEM analysis this is not the case as discussed in the following section 5, where it is clear that electrocatalyst coats well the inner porous electrode surface. However, due to the dense microstructure the electrocatalyst coating may be very thin, which limits the ionic conductivity. Furthermore, from previous TEM studies of Ni:CGO electrocatalyst infiltration on FeCr:YSZ anode backbone it is evident that interdiffusion of significant amounts of Fe into the Ni:CGO electrocatalyst coating takes place [17]. This will change the ionic conductivity and electrochemical properties. It is believed that this Fe originates from the initial formation of a corrosion protective Cr_2O_3 scale on the FeCr metal particles during the very initial electrochemical testing of the cells. For the present case LSFNT is tailored to exsolute Ni and Fe nanoparticles and it is also unknown whether other elements interdiffuse into the electrocatalyst coating. Thin electrocatalyst coatings are in particular expected to be sensitive to such interdiffusion phenomena, which will change the chemical composition. For further knowledge and clarification detailed TEM studies are needed. Fig. 3B shows visualization of the impedance data in terms of distribution of relaxation times (DRT) [18]. From the DRT plot it is possible to see that in particular one process changes from cell to cell. For the best performing cell C with similar performance as DTU SoA cells it is possible to see that the process is located at approx. 100 Hz at 650 °C. From previous detailed impedance studies of DTU SoA cell anodes, it has been shown, that the process at 100 Hz is the anode transmission line response representing the anode electrochemical reaction process [10]. From the DRT plot it can be seen that this process increases and shifts to lower frequencies in accordance with the

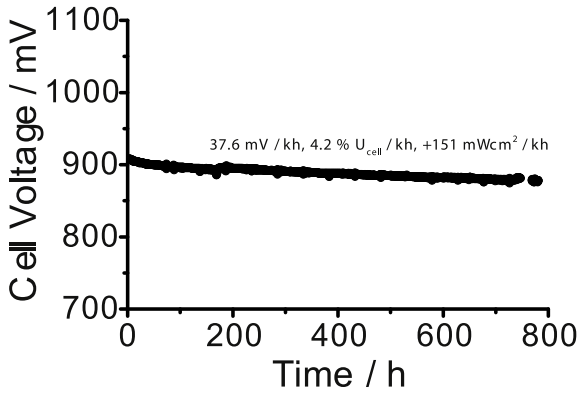

Fig. 4. Galvanostatic durability test of cell B with the anode backbone composition 55% LSFNT/40% FeCr/5% ScYSZ at 650 °C and 0.25Acm^{-2} with air as oxidant and 4% humidified hydrogen as fuel.

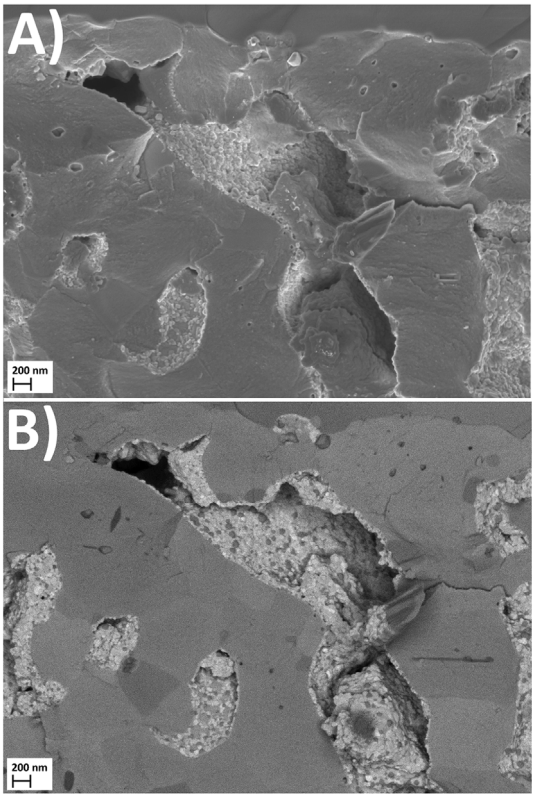

Fig. 5. A) Micrograph with Inlens SE detector of cell A. **B)** Micrograph of cell A by use of an energy selective backscatter detector where Ni particles appear dark and CGO particles appear bright.

performance ranking of the studied cells. This is in agreement with expectations.

4.3. Durability testing

In Fig. 4 galvanostatic long term testing of cell B is shown. The test is performed at a current density of 0.25 Acm^{-2}. As with specification of performance there are many ways degradation rates can be specified as illustrated in Fig. 4. The most appropriate degradation rate specification depends on the given context. From the figure a degradation rate of 4.2% U_{cell}/kh can be seen, which is somewhat higher than what we previously have reported for DTU SoA cell with FeCr/YSZ anode backbones. For the DTU SoA cells, the best degradation rates observed is approximately slightly above 1% U_{cell}/kh both at low (~10%) and high (> 70%) fuel utilization [2,11]. Considering it is a first attempt with no further optimization it seems fairly promising.

5. Overall discussion

As briefly mentioned in the introduction we have previously explored the use of infiltrated $SrTiO_3$:FeCr anodes for MS-SOFC [8]. In here, the same $SrTiO_3$:FeCr anode cells had at 650 °C an ASR_{corr} = 0.72 Ωcm^2 in button cell testing (active area 0.5 cm^2) and ASR_{corr} = 1.23 Ωcm^2 in single cell testing (active area 16 cm^2). In comparison to these results, the performance of the anodes within the present study are in all cases superior. Furthermore, from a processing point of view, adhesion between functional layers, electronic and ionic conductivity point of view, LSFNT based anodes are superior in comparison to $SrTiO_3$ based anodes. In addition, as previously mentioned it was found that the infiltrated Ni:CGO electrocatalyst did not seem to be stable as a coating on the $SrTiO_3$ surface, since clear island like structures of Ni:CGO was observed. Therefore similar investigations of the Ni:CGO

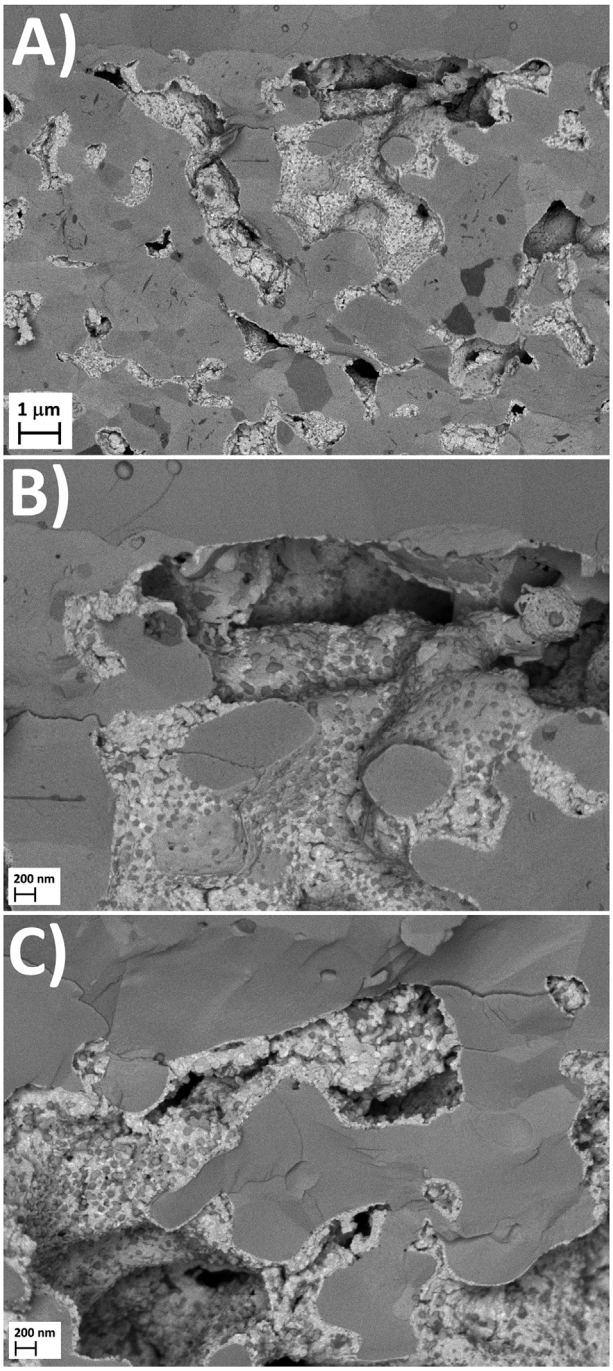

Fig. 6. Micrographs by use of an energy selective backscatter detector where Ni particles appear dark and CGO particles appear bright **A)** Overview of infiltrated Ni:CGO electrocatalyst distribution in cell A **B)** Zoom in on Ni and CGO particle distribution with the infiltrated electrocatalyst coating of cell A with the densest anode microstructure. **C)** Zoom in on Ni and CGO particle distribution with the infiltrated electrocatalyst coating of cell C with the most open anode microstructure.

electrocatalyst coating on the inner surface of the present studied anodes was performed. These studies were also performed to see how the infiltration is assimilated by the various microstructures of the studied anodes. Representative results are shown in Figs. 5 and 6. In Fig. 5A an image acquired by use of an Inlens secondary electron (SE) detector (with no contrast between the Ni and CGO infiltrates) of cell A anode is shown. In Figs. 5B and 6 images acquired by use of an energy selective backscatter detector are shown, where Ni particles appear dark and CGO appears bright. Comparison of Fig. 5A and B of cell A anode shows

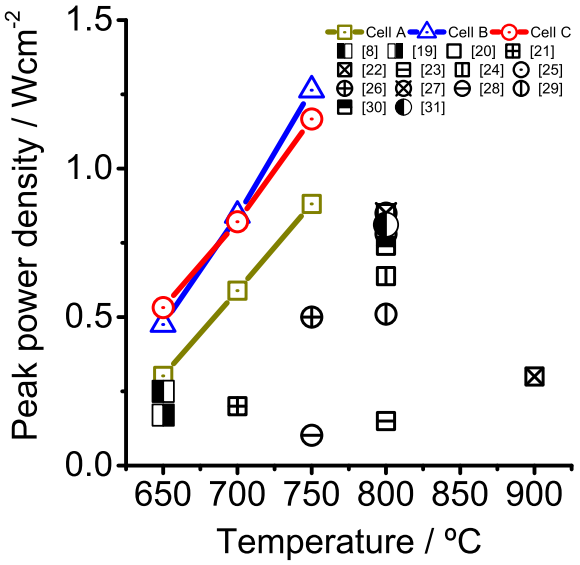

Fig. 7. Literature comparison of peak power densities of cells with different combinations of ceramic anode backbone materials and electrocatalyst infiltrations. Further details on the cell specifications are given in Table 2.

that the image 5B provides much more information. Despite the relatively dense microstructure of the all ceramic anode backbone of cell A, the images in Figs. 5 and 6A and 6B shows a uniform and apparent stable coverage of percolated Ni:CGO electrocatalyst on the inner anode surfaces of cell A and in general all cells A, B and C. In addition it is possible to see the individual CGO grains (bright) and Ni particles (dark) and thus the distribution hereof. It is seen that the Ni particles are well and evenly distributed. Figs. 5B and 6C show that the Ni particles are below 50 nm in size, which is in agreement with previous Transmission Electron Microscopy (TEM) studies of Ni:CGO electrocatalyst coatings on FeCr/YSZ anode based backbones [17]. However, in Fig. 6B most Ni particles are below 50 nm, but there are some larger particles up to approx. 150 nm close to the electrolyte interface. A more open microstructure is expected to lead to a larger electrocatalyst loading and therefore thicker coating after an equal number of infiltration cycles compared to a denser microstructure. From comparison of Fig. 6B (cell A densest microstructure) and Fig. 6C (cell C most open microstructure) it seems to be the case, but it is difficult to say with certainty. However, if the electrocatalyst coating becomes thinner than the "normal" Ni growth (< 50 nm) within a thick Ni:CGO coating, the Ni particles are no longer surrounded and stabilized by CGO, which would lead to an enhanced Ni growth. This could explain the larger Ni particles up to approx. 150 nm observed in Fig. 6B of cell A with the densest microstructure. TEM analysis is needed to acquire further insight into the electrocatalyst thickness and the anode backbone element interdiffusion along with Ni and GCO grain size distribution.

The benefit of having an anode material as LSFNT with nanoparticle ex-solution properties is at present not clear. From a processing point of view, one benefit could be a better adhesion between the anode/electrolyte and the anode/support layers. Exsoluted Ni and Fe nanoparticles are expected to have a high sintering activity or at the metal support interface possibility of interdiffusion. This could improve the bonding between the layers. In contrast, from an electrochemical point of view it is perhaps difficult to see a benefit of having exsoluted Ni and Fe nanoparticles on the surface since a nanostructured electrocatalyst coating is subsequently deposited by infiltration. On the contrary, exsoluted nanoparticles on the anode backbone surface may destabilize the infiltrated electrocatalyst coating and/or chemically alter it due to interdiffusion. A too high metal electrocatalyst loading e.g. Ni may lead to agglomeration and undesirable additional Ni particle growth. Recently, the performance of a non-infiltrated composite anode consisting of

Table 2
Specification of anode backbones and the infiltrated electrocatalysts from the comparison of the cell performances in Fig. 7. Abbreviations are as follows C-GO = GDC = gadolinium doped ceria, SDC = samarium doped ceria, YSZ = yttria doped zirconia.

Anode backbone	Infiltrated electrocatalyst	Ref.
$Sr_{0.99}Ti_{0.9}Nb_{0.1}O_3$/FeCr	CGO + Ni	[8]
$La_{0.2}Sr_{0.8}Ti_{0.9}Ni_{0.1}O_{3-\delta}$/YSZ	None	[19]
$(Sr_{0.89}Y_{0.07})_{0.91}TiO_{2.91}$/YSZ	Ni	[20]
$La_{0.3}Sr_{0.7}TiO_3$	CeO_2 + Cu	[21]
$La_{0.20}Sr_{0.25}Ca_{0.45}TiO_3$	CeO_2 + Ni	[22]
$La_{0.4}Sr_{0.6}Ti_{0.8}Mn_{0.2}O_3$	Pd + CeO_2	[23]
$La_{0.2}Sr_{0.8}Ti_{0.98}Co_{0.02}O_3$	CGO + Ni	[24]
$La_{0.3}Sr_{0.7}TiO_3$	CeO_2 + Pd	[25]
$La_{0.2}Sr_{0.7}TiO_3$	GDC + Cu	[26]
$La_{0.2}Sr_{0.8}TiO_3$	NiO–SDC + NiO–YSZ	[27]
$La_{0.3}Sr_{0.7}TiO_3$	Ni/YSZ	[28]
$Sr_{0.88}Y_{0.08}TiO_3$/YSZ	CeO_2 + Ru	[29]
YSZ	Mo-doped $SrFeO_{3-\delta}$	[30]
$Sr_2MgMoO_{6-\delta}$	None	[31]

$La_{0.2}Sr_{0.8}Ti_{0.9}Ni_{0.1}O_{3-\delta}$ (LSTN) and YSZ have been reported [19]. LSTN was reported to have Ni exsolution capability, which is expected to improve the electrocatalytic activity of the composite. However, the performance with a peak power density of 0.17 Wcm^{-2} at 650 °C is inferior in comparison to the performance of the present studied infiltrated anodes.

Fig. 7 is an attempt to put the performance of the studied anodes within the present study into a larger context. In Fig. 7, selected performances reported within the most recent reviews [3,4] is plotted of cells with non-infiltrated and infiltrated all ceramic titanate based anodes. In addition some further selected literature performance data are also plotted in Fig. 7 along with the results of the present study. The performance data are selected such that it gives a broad variation in combinations of backbone materials and designs along with different types of infiltrated electrocatalysts. In Table 2 an overview and further details is provided of the cell anode materials and electrocatalysts plotted in Fig. 7. The comparison is not meant as a complete literature review since this is outside the scope of the present paper. However, the comparison is considered representative for the most promising results reported. Taking the temperature into consideration, the results of the present study are from the comparison performance wise quite encouraging. Cell A poses the fairest comparison as this is an all ceramic anode (95% LSFNT/5% ScYSZ). Despite cell A performs the worst of the studied anodes it is still in the context of the comparison of Fig. 7 well performing. The data plotted are the fuel utilization corrected data in Fig. 2 summarized in Table 1 as the compared literature data are mainly performance evaluated at button cell level. Nonetheless, even the performance data with significant FU does not change the conclusions of well performing LSFNT based anodes of the present study. The comparison is by nature not completely fair as the cell performance also depends on the other cell components. Nonetheless, it illustrates the large potential of the present studied anodes, especially when considering, that the reported results are a first design without any further optimization.

6. Conclusions

The performance of Ni:CGO infiltrated metal supported solid oxide fuel cells with A site deficient lanthanum doped strontium titanate $La_{0.4}Sr_{0.4}Fe_{0.03}Ni_{0.03}Ti_{0.94}O_3$ based anodes were studied. The studied anode compositions of the cells were as follows 95% LSFNT/5% ScYSZ, 55% LSFNT/40% FeCr/5% ScYSZ and 20% LSFNT/60% FeCr/20% ScYSZ. Extrapolated peak power densities at 700 °C were as follows 0.503 Wcm^{-2} (FU 33%), 0.770 Wcm^{-2} (FU 51%) and 0.73 Wcm^{-2} (FU 48%). Taking the temperature into consideration the performances are among the best reported for redox stable and corrosion resistant

alternatives to the conventional Ni:YSZ composite solid oxide cell electrode. In addition, up scalability to 12 cm × 12 cm sized cells were demonstrated, where LSFNT showed good processing properties in terms of sinterability and adhesion with the electrolyte and metal support layer. Finally, LSFNT seems to possess sufficient electronic conductivity and showed very good surface wetting properties towards the infiltrated Ni:CGO electrocatalyst coating.

Acknowledgements

Financial support by the EU project METSAPP (FP7-278257) and Energinet.dk under the project ForskEL 2012-1-10806 is gratefully acknowledged.

References

[1] M.C. Tucker, Progress in metal-supported solid oxide fuel cells: a review, J. Power Sources 195 (2010) 4570–4582, http://dx.doi.org/10.1016/j.jpowsour.2010.02.035.

[2] B.J. McKenna, N. Christiansen, R. Schauperl, P. Prenninger, J. Nielsen, P. Blennow, T. Klemensø, S. Ramousse, A. Kromp, A. Weber, Advances in metal supported cells in the METSOFC EU consortium, Fuel Cells 13 (2013) 592–597, http://dx.doi.org/10.1002/fuce.201200185.

[3] M.C. Verbraeken, T. Ramos, K. Agersted, Q. Ma, C.D. Savaniu, B.R. Sudireddy, J.T.S. Irvine, P. Holtappels, F. Tietz, Modified strontium titanates: from defect chemistry to SOFC anodes, RSC Adv. 5 (2014) 1168–1180, http://dx.doi.org/10.1039/C4RA09751C.

[4] X. Zhou, N. Yan, K.T. Chuang, J. Luo, Progress in La-doped $SrTiO_3$ (LST)-based anode materials for solid oxide fuel cells, RSC Adv. 4 (2014) 118–131, http://dx.doi.org/10.1039/C3RA42666A.

[5] B.R. Sudireddy, K. Agersted, Sintering and electrical characterization of La and Nb Co-doped SrTiO3 electrode materials for solid oxide cell applications, Fuel Cells 14 (2014) 961–965, http://dx.doi.org/10.1002/fuce.201400017.

[6] D. Neagu, G. Tsekouras, D.N. Miller, H. Ménard, J.T.S. Irvine, In situ growth of nanoparticles through control of non-stoichiometry, Nat. Chem. 5 (2013) 916–923, http://dx.doi.org/10.1038/nchem.1773.

[7] G. Tsekouras, D. Neagu, J.T.S. Irvine, Step-change in high temperature steam electrolysis performance of perovskite oxide cathodes with exsolution of B-site dopants, Energy Environ. Sci. 6 (2012) 256–266, http://dx.doi.org/10.1039/C2EE22547F.

[8] P. Blennow, B.R. Sudireddy, Å.H. Persson, T. Klemensø, J. Nielsen, K. Thydén, Infiltrated SrTiO3:FeCr-based anodes for metal-supported SOFC, Fuel Cells 13 (2013) 494–505, http://dx.doi.org/10.1002/fuce.201200176.

[9] P. Blennow, J. Hjelm, T. Klemensø, Å.H. Persson, S. Ramousse, M. Mogensen, Planar metal-supported SOFC with novel cermet anode, Fuel Cells 11 (2011) 661–668, http://dx.doi.org/10.1002/fuce.201100029.

[10] J. Nielsen, T. Klemensø, P. Blennow, Detailed impedance characterization of a well performing and durable Ni:CGO infiltrated cermet anode for metal-supported solid oxide fuel cells, J. Power Sources 219 (2012) 305–316, http://dx.doi.org/10.1016/j.jpowsour.2012.07.031.

[11] T. Klemensø, J. Nielsen, P. Blennow, Å.H. Persson, T. Stegk, B.H. Christensen, S. Sønderby, High performance metal-supported solid oxide fuel cells with Gd-doped ceria barrier layers, J. Power Sources 196 (2011) 9459–9466, http://dx.doi.org/10.1016/j.jpowsour.2011.07.014.

[12] M. Mogensen, P.V. Hendriksen, S.C. Singhal, K. Kendall (Eds.), High Temperature Solid Oxide Fuel Cells: Fundamentals, Design, and Applications, Elsevier Advanced Technology, Oxford, 2003, p. 261.

[13] J. Nielsen, J. Hjelm, Impedance of SOFC electrodes: a review and a comprehensive case study on the impedance of LSM: YSZ cathodes, Electrochim. Acta 115 (2014) 31–45, http://dx.doi.org/10.1016/j.electacta.2013.10.053.

[14] J. Nielsen, B.R. Sudireddy, A. Hagen, Å.H. Persson, Performance factors and sulfur tolerance of metal supported solid oxide fuel cells with nanostructured Ni:GDC infiltrated anodes, J. Electrochem. Soc. 163 (2016) F574–F580, http://dx.doi.org/10.1149/2.1081606jes.

[15] M.C. Tucker, Development of high power density metal-supported solid oxide fuel cells, Energy Technol. 5 (2017) 1–8, http://dx.doi.org/10.1002/ente.201700242.

[16] J. Nielsen, P.S. Jørgensen, Estimation of current constriction losses via 3D tomography reconstructions in electrochemical devices: a case study of a solid oxide cell electrode/electrolyte interface, Electrochim. Acta 252 (2017) 387–396, http://dx.doi.org/10.1016/j.electacta.2017.08.100.

[17] R. Knibbe, H.-J. Wang, P. Blennow, K. Thydén, Å.H. Persson, L. Mikkelsen, T. Klemensø, Oxidation in ceria infiltrated metal supported SOFCs – a TEM investigation, J. Power Sources 228 (2013) 75–82, http://dx.doi.org/10.1016/j.jpowsour.2012.11.051.

[18] H. Schichlein, A.C. Müller, M. Voigts, A. Krügel, E. Ivers-Tiffée, Deconvolution of electrochemical impedance spectra for the identification of electrode reaction mechanisms in solid oxide fuel cells, J. Appl. Electrochem. 32 (2002) 875–882, http://dx.doi.org/10.1023/A:1020599525160.

[19] A.M. Dayaghi, K.J. Kim, S. Kim, J. Park, S.J. Kim, B.H. Park, G.M. Choi, Stainless steel-supported solid oxide fuel cell with $La_{0.2}Sr_{0.8}Ti_{0.9}Ni_{0.1}O_{3-\delta}$/yttria-stabilized zirconia composite anode, J. Power Sources 324 (2016) 288–293, http://dx.doi.org/10.1016/j.jpowsour.2016.05.076.

[20] Q. Ma, F. Tietz, A. Leonide, E. Ivers-Tiffée, Anode-supported planar SOFC with high performance and redox stability, Electrochem. Commun. 12 (2010) 1326–1328, http://dx.doi.org/10.1016/j.elecom.2010.07.011.

[21] K. Ahn, S. Jung, J.M. Vohs, R.J. Gorte, A support layer for solid oxide fuel cells, Ceram. Int. 33 (2007) 1065–1070, http://dx.doi.org/10.1016/j.ceramint.2006.03.012.

[22] M.C. Verbraeken, B. Iwanschitz, A. Mai, J.T.S. Irvine, Evaluation of Ca doped $La_{0.2}Sr_{0.7}TiO_3$ as an alternative material for use in SOFC anodes, J. Electrochem. Soc. 159 (2012) F757–F762, http://dx.doi.org/10.1149/2.001212jes.

[23] J.H. Kim, D. Miller, H. Schlegl, D. McGrouther, J.T.S. Irvine, Investigation of microstructural and electrochemical properties of impregnated (La,Sr)(Ti,Mn)$O_{3\pm\delta}$ as a potential anode material in high-temperature solid oxide fuel cells, Chem. Mater. 23 (2011) 3841–3847, http://dx.doi.org/10.1021/cm2007318.

[24] K.B. Yoo, B.H. Park, G.M. Choi, Stability and performance of SOFC with $SrTiO_3$-based anode in CH_4 fuel, Solid State Ionics 225 (2012) 104–107, http://dx.doi.org/10.1016/j.ssi.2012.05.017.

[25] S. Lee, G. Kim, J.M. Vohs, R.J. Gorte, SOFC anodes based on infiltration of $La_{0.3}Sr_{0.7}TiO_3$, J. Electrochem. Soc. 155 (2008) B1179–B1183, http://dx.doi.org/10.1149/1.2976775.

[26] C.D. Savaniu, J.T.S. Irvine, La-doped $SrTiO_3$ as anode material for IT-SOFC, Solid State Ionics 192 (2011) 491–493, http://dx.doi.org/10.1016/j.ssi.2010.02.010.

[27] M.R. Pillai, I. Kim, D.M. Bierschenk, S.A. Barnett, Fuel-flexible operation of a solid oxide fuel cell with $Sr_{0.8}La_{0.2}TiO_3$ support, J. Power Sources 185 (2008) 1086–1093, http://dx.doi.org/10.1016/j.jpowsour.2008.07.063.

[28] M.A. Buccheri, J.M. Hill, Methane electrochemical oxidation pathway over a Ni/YSZ and $La_{0.3}Sr_{0.7}TiO_3$ bi-layer SOFC anode, J. Electrochem. Soc. 159 (2012) B361–B367, http://dx.doi.org/10.1149/2.001204jes.

[29] H. Kurokawa, L. Yang, C.P. Jacobson, L.C. De Jonghe, S.J. Visco, Y-doped $SrTiO_3$ based sulfur tolerant anode for solid oxide fuel cells, J. Power Sources 164 (2007) 510–518, http://dx.doi.org/10.1016/j.jpowsour.2006.11.048.

[30] Y. Zhou, X. Meng, X. Liu, X. Pan, J. Li, X. Ye, H. Nie, C. Xia, S. Wang, Z. Zhan, Novel architectured metal-supported solid oxide fuel cells with Mo-doped $SrFeO_{3-\delta}$ electrocatalysts, J. Power Sources 267 (2014) 148–154, http://dx.doi.org/10.1016/j.jpowsour.2014.04.157.

[31] Y.-H. Huang, R.I. Dass, Z.-L. Xing, J.B. Goodenough, Double perovskites as anode materials for solid-oxide fuel cells, Science 312 (2006) 254–257, http://dx.doi.org/10.1126/science.1125877.